The compressive and shear responses of corrugated and diamond lattice materials

F. Côté [a], V.S. Deshpande [a,*], N.A. Fleck [a], A.G. Evans [b]

[a] *Engineering Department, Cambridge University, Trumpington Street, Cambridge CB2 1PZ, UK*
[b] *Materials Department, University of California, Santa Barbara, CA 93106-5050, USA*

Abstract

Corrugated and diamond lattice materials have been manufactured as the cores of sandwich panels by slotting together stainless steel sheets and then brazing together the assembly. The out-of-plane compressive, transverse shear and longitudinal shear responses of the corrugated cores have been measured at three relative densities $0.03 < \bar{\rho} \leqslant 0.10$ and compared with analytical and finite element (FE) predictions. Finite element models are in good agreement with the experimental measurements while the analytical models over-predict the measured strength due to a neglect of manufacturing imperfections. The out-of-plane compressive and transverse shear responses of the diamond cores have also been measured at three relative densities $0.08 \leqslant \bar{\rho} \leqslant 0.25$. The compressive strengths are sensitive to the aspect ratio of the specimens for $L/H < 4$ and again are below the analytical predictions due to imperfections. The longitudinal shear strength and energy absorption compare favorably with competing core topologies but the prismatic corrugated and diamond cores are weaker than the pyramidal and square-honeycomb under compression and transverse shear.
© 2005 Elsevier Ltd. All rights reserved.

Keywords: Corrugated cores; Diamond cores; Plastic buckling; Energy-absorption; Sandwich panels

1. Introduction

Micro-architectured materials are being pursued for various multi-functional applications, because of their ability to support loads, dissipate heat and change shape (Evans et al., 2001). Two basic architectures include trusses and prismatics (Deshpande et al., 2001; Wadley et al., 2003).

---

* Corresponding author. Tel.: +44 1223 332664; fax: +44 1223 332662.
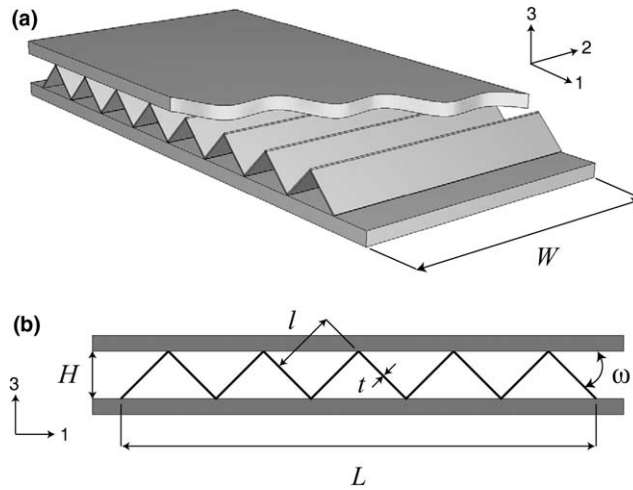*E-mail address:* vsd@eng.cam.ac.uk (V.S. Deshpande).

Fig. 1. (a) Isometric view and (b) front view of the corrugated core. The geometrical parameters used to characterise the specimens and the core topology are marked along with the co-ordinate system employed. Out-of-plane compression is along the x_3-direction, transverse shear is in the 1–3 plane along the x_1-direction, and longitudinal shear is in the 2–3 plane along the x_2-direction.
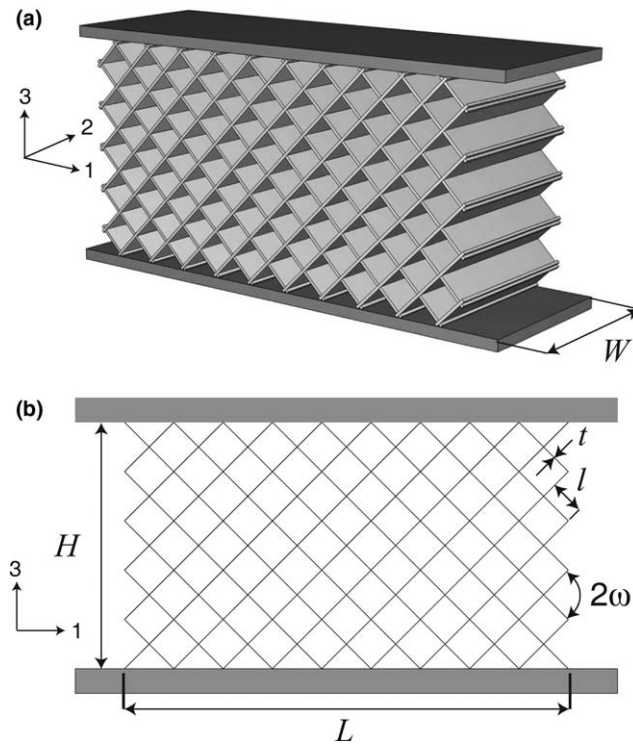

Fig. 2. (a) Isometric view and (b) front view of the diamond core. The geometrical parameters used to characterise the specimens and the core topology are marked along with the co-ordinate system employed. Out-of-plane compression is along the x_3-direction, and transverse shear is in the 1–3 plane along the x_1-direction.

Prismatics, such as the Y-core (Naar et al., 2001) and NavTruss (Astech Inc.), are preferred in marine sandwich construction for two reasons (i) they are straightforward to manufacture on large length scales by a welding route and (ii) the high longitudinal stretching and shear strength of the cores makes them ideal for application in sandwich beams. For example, Fleck and Deshpande (2004) and Xue and Hutchinson (2004) have shown that prismatic geometries are near optimal for shock resistant sandwich construction. More recently, Valdevit et al. (2004) have revealed that the structural attributes of the prismatic cores can be combined with their thermal characteristics to devise actively cooled multifunctional panels. The aim of this study is to investigate the quasi-static response of two prismatic sandwich cores; the corrugated and diamond cores, as shown in Figs. 1 and 2, respectively.

The outline of the paper is as follows. The slotting technique used to manufacture the corrugated and diamond cores is described in Section 2 while the measured compressive and shear responses of the corrugated and diamond cores are compared with analytical and finite element predictions in Sections 3 and 4. Finally, the strength and energy absorption capacities of these cores are compared in Section 5 with those of competing core topologies such as the square-honeycomb and pyramidal core.

2. Materials and manufacturing route

Corrugated cores and diamond cores as sketched in Figs. 1 and 2, respectively, were manufactured from 304 stainless steel sheets, thickness $t = 0.3$ mm. The slotting technique shown in Fig. 3 was used to produce both types of core, following the method developed by Côté et al. (2004) for square-honeycombs. Stainless steel sheets were cropped into rectangles, and then cross-slotted by electro-discharge machining (EDM). The slots were of width $\Delta t = 0.305$ mm, of spacing l and were cut to half-depth of the sheet. The sheets were assembled in a $\pm 45°$ array in order to produce sandwich panels of length L, thickness H, and width W, as sketched in Fig. 1 for the corrugated core and in Fig. 2 for the diamond core. The clearance of 5 µm between the sheets and slots facilitated assembly while providing a sufficiently tight fit to assure stability. The braze alloy Ni–Cr 25-P10 (wt.%) was applied uniformly over the sheets of the core (increasing the sheet thickness to $t = 0.31$ mm) and the inner surface of the face-sheets. The assembly (core and face-sheets) was brazed together in a vacuum furnace at 1075 °C in a dry argon atmosphere at 0.03–0.1 mbar. Capillarity forces were sufficient to draw the braze into the joints, resulting in an excellent bond.

The relative density of the corrugated and diamond core specimens, made from sheets of thickness t with a cell size l is, to first order, given by
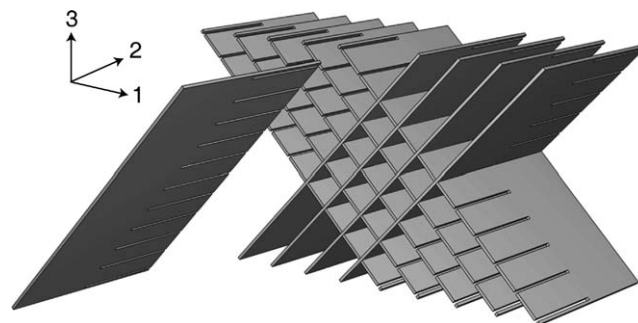
$$\bar{\rho} = \frac{2t}{l \sin 2\omega},$$

(1)

Fig. 3. Sketch of the slotting procedure used to manufacture the cores.

where ω is the angle of corrugated core as shown in Figs. 1b and 2b. In the present study, all specimens have cells with $\omega = \pi/4$.

2.1. Tests on the corrugated cores

Corrugations were machined onto the inner surface of the face-sheets in order to ensure good bonding (see Fig. 4a). The cores were tested in out-of-plane compression and in transverse shear at the three relative densities $\bar{\rho} = 0.036$, 0.05 and 0.10, using width $W = 60$ mm and aspect ratio $L/H = 12$. Additional longitudinal shear tests were performed on the corrugated core specimens; it sufficed to test narrow specimens comprising three corrugations in the 1–3 plane such that $L = 6H$, and a width to height ratio $W/H = 12$.

2.2. Tests on the diamond cores

Out-of-plane compression and transverse shear tests were performed on the diamond cores of relative density $\bar{\rho} = 0.08$, 0.19 and 0.25, and aspect ratios $L/H = 2$, 4 and 8. Each had five cells along the core height direction (the x_3-direction), and a width to height ratio, $W/H = 1$. The specimens employed in the transverse shear tests contained corrugations on the inner surfaces of the face-sheets (see Fig. 4b). No such corrugations were required for the compression tests, flat 3 mm thick stainless-steel face-sheets sufficed (Fig. 4c). No longitudinal shear tests were performed as such tests required specimens with aspect ratios $W/H \geqslant 8$: the manufacturing and laboratory testing difficulties associated with such large specimens were impractical.
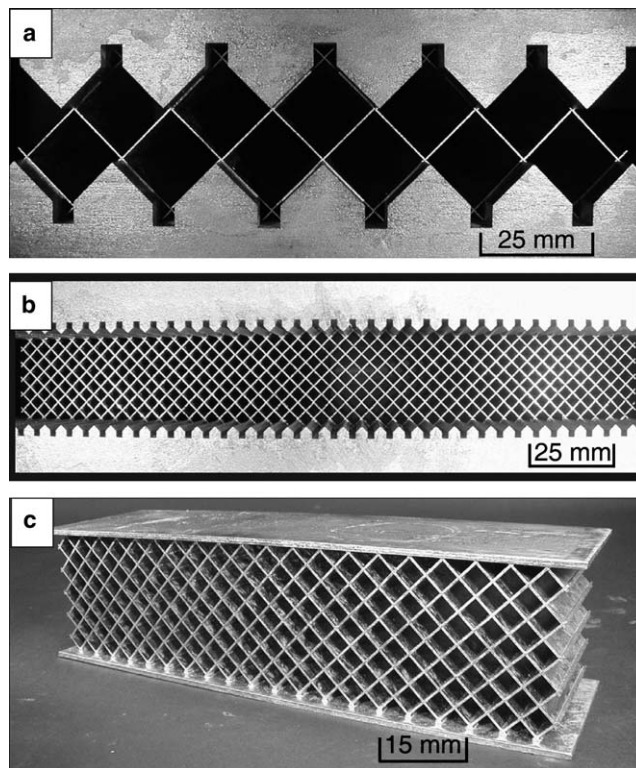

Fig. 4. Photographs of the as-manufactured specimens: (a) corrugated core specimen, $\bar{\rho} = 0.036$; (b) diamond core specimen, $\bar{\rho} = 0.19$, $L/H = 8$ used in the transverse shear tests; and (c) diamond core specimen, $\bar{\rho} = 0.19$, $L/H = 4$ used in the out-of-plane compression tests.
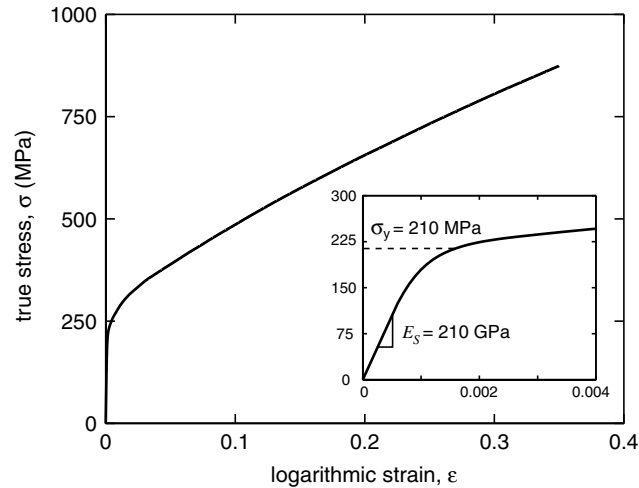
Fig. 5. Measured tensile stress versus strain curve of the as-brazed 304 stainless steel at a strain rate of $10^{-4}\,\mathrm{s}^{-1}$.

2.3. Properties of the parent material

Tensile specimens of dog-bone geometry were cut from the as-received 304 stainless steel sheets and were subjected to the same brazing cycle as that used to manufacture the corrugated and diamond cores. The measured true tensile stress σ versus logarithmic strain ε response shown in Fig. 5 is adequately represented by an elastic–plastic solid of Young's modulus $E_s = 210$ GPa, 0.1% offset yield strength $\sigma_y = 210$ MPa and linear hardening with modulus $E_t \equiv d\sigma/d\varepsilon \approx 2.1$ GPa.

2.4. Test protocol

The compressive and shear responses of the corrugated and diamond cores were measured in a 150 kN screw driven test machine at a nominal applied strain-rate of $10^{-4}\,\mathrm{s}^{-1}$. The load was measured by the load cell of the test machine and was used to define the nominal stress, while laser extensometers were employed to measure the compressive and shear strains. The compression and shearing directions are described using the co-ordinate systems sketched in Figs. 1 and 2.

The out-of-plane compressive response (σ_{33} versus ε_{33}) was measured by compressing the specimens between two rigid platens. Linear bearings between the platens and the face-sheets of the specimens ensured frictionless loading. The transverse shear (σ_{31} versus γ_{31}) and longitudinal shear (σ_{32} versus γ_{32}) responses were measured via single lap shear tests conforming to the ASTM Standard C273-94 (1994) for shear tests on sandwich cores. The length to thickness ratio of the corrugated and diamond core specimens in the shear tests was taken to be 12 and 8, respectively.

3. Corrugated cores

The out-of-plane compressive responses (Fig. 6a–c) all display a peak stress followed by a strong softening response. Densification of the core was not investigated because the corrugations on the inner surfaces of the face-sheets permitted nominal compressive strains, $\varepsilon_{33} > 1$. The peak stress increases systematically with increasing $\bar{\rho}$. Images at different levels of compression (Fig. 7) indicate that the peak
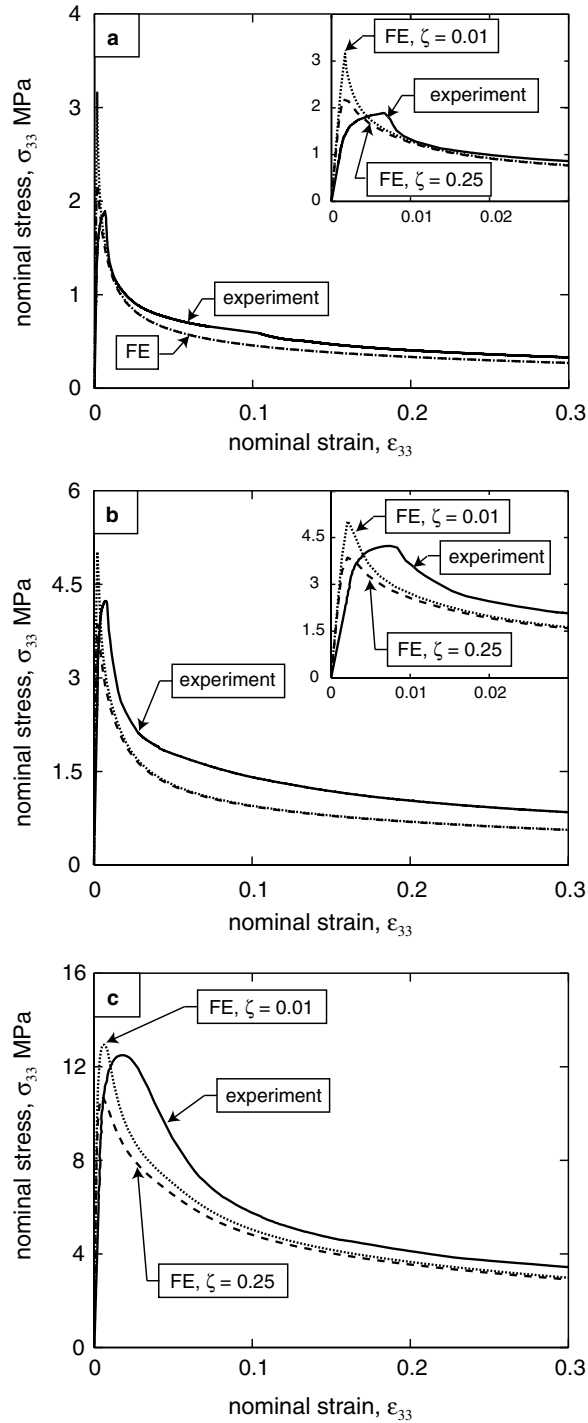
Fig. 6. Measured responses and finite element predictions of the corrugated core specimens in out-of-plane compression: (a) $\bar{\rho} = 0.036$, (b) $\bar{\rho} = 0.05$ and (c) $\bar{\rho} = 0.10$.
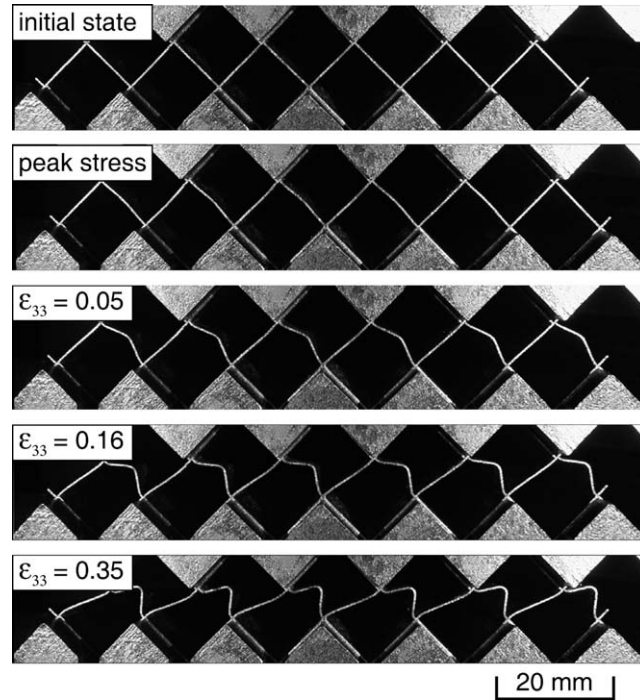
Fig. 7. Photographs of the $\bar{\rho} = 0.05$ corrugated core showing the deformation mode during tests in out-of-plane compression.

load is governed by buckling of the constituent struts while the subsequent softening is associated with the post-buckling response.

The transverse shear responses (Fig. 8) also exhibit a peak, occurring at stresses similar in magnitude to those found for compression. Images at selected levels of engineering shear strain (Fig. 9) suggest that the peak load is now governed by plastic buckling of one of the constituent struts. The exception is the peak at $\bar{\rho} = 0.10$, which is governed by tearing of the core from the face-sheet; causing the post-peak softening to be significantly less than in the other cases.

In longitudinal shear (Fig. 10) the peak stresses exceed those in compression or transverse shear and the post-peak softening is more moderate. The $\bar{\rho} = 0.10$ specimen has no peak: instead it continues to harden up to the largest strain investigated ($\gamma_{32} = 0.6$). Images (Fig. 11) of the deformation indicate that it involves "wrinkling" of the sheets comprising the core. Typically five wrinkles form along the width W of the specimens at $\approx 45°$ to the shearing direction. The amplitude of the wrinkles increases with increasing strain.

3.1. Analytical models for the compressive and shear response

At small t/l, the contribution to the overall stiffness from bending of the constituent struts is negligible compared to that from stretching. Thus, for deriving a simple expression for the stiffness we assume the struts to be pin-jointed to the face-sheets whereupon the out-of-plane Young's and transverse shear moduli are given by

$$E_{33} = \frac{E_s}{1 - v^2} \bar{\rho} \sin^4 \omega, \tag{2}$$

and

$$G_{31} = \frac{E_s}{1 - v^2} \frac{\bar{\rho}}{4} \sin^2 2\omega, \tag{3}$$
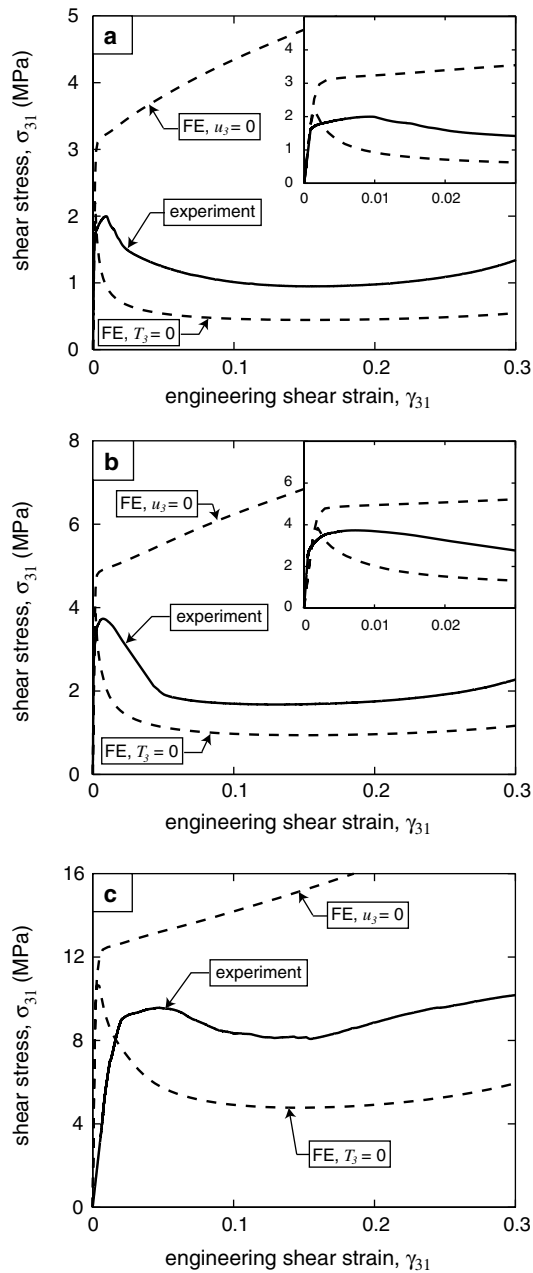

Fig. 8. Measured responses and finite element predictions of the corrugated core specimens in transverse shear: (a) $\bar{\rho} = 0.036$, (b) $\bar{\rho} = 0.05$ and (c) $\bar{\rho} = 0.10$. Finite element predictions for both the fully constrained grip condition ($u_3 = 0$) and the unconstrained grip condition ($T_3 = 0$) are included (an imperfection of amplitude $\zeta = 0.25$ and specified by Eq. (13) was employed in the FE calculations).
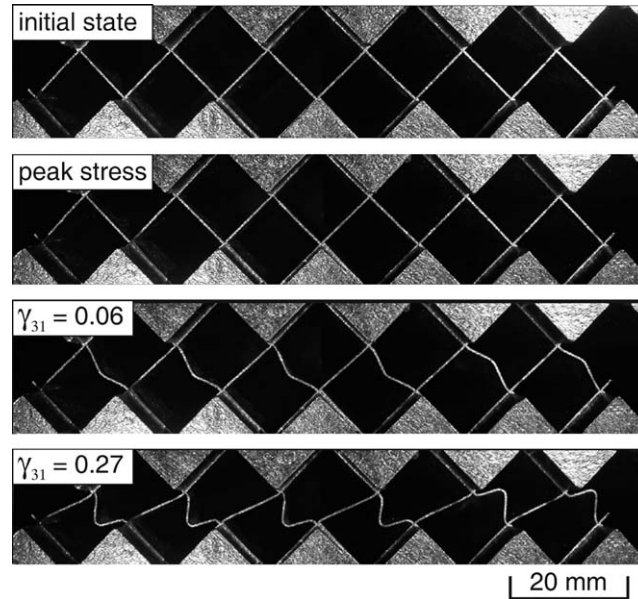
Fig. 9. Photographs of the $\bar{\rho} = 0.05$ corrugated core showing the deformation mode during tests in transverse shear.

respectively, where E_s and v are the Young's modulus and Poisson's ratio of the constituent solid. Note that since $W \gg l$, plane-strain conditions are established and thus the factor $1 - v^2$ has been introduced. Under longitudinal shear, the engineering shear strain γ_{23} is related to that in wall of the corrugated core constituent struts γ_w via

$$\gamma_{32} = \frac{\gamma_w}{\sin \omega}. \tag{4}$$

An energy balance gives the effective shear modulus G_{32} of the corrugated core as

$$G_{32} = \frac{E_s}{2(1 + v)} \bar{\rho} \sin^2 \omega. \tag{5}$$

We proceed to develop analytical models for the peak strength of the corrugated core. For small t/l, an equilibrium analysis dictates that the peak compressive and transverse shear strengths are given by

$$\sigma_{33}^p = \sigma_c \bar{\rho} \sin^2 \omega, \tag{6}$$

and

$$\sigma_{31}^p = \sigma_c \frac{\bar{\rho}}{2} \sin 2\omega, \tag{7}$$

respectively, where σ_c is the maximum compressive strength of the constituent struts. This maximum compressive stress is set by either elastic or plastic buckling of the struts as given by the Euler elastic buckling and Shanley plastic bifurcation stresses (Shanley, 1947),

$$\sigma_c = \begin{cases} \dfrac{k^2 \pi^2 E_s}{12(1 - v^2)} \left(\dfrac{t}{l}\right)^2 & \text{if } \dfrac{t}{l} < \sqrt{\dfrac{8\sqrt{3}(1 - v^2)\sigma_y}{\pi^2 k^2 E_s}}, \\[4mm] \dfrac{k^2 \pi^2 E_t}{12} \left(\dfrac{t}{l}\right)^2 & \text{otherwise,} \end{cases} \tag{8}$$
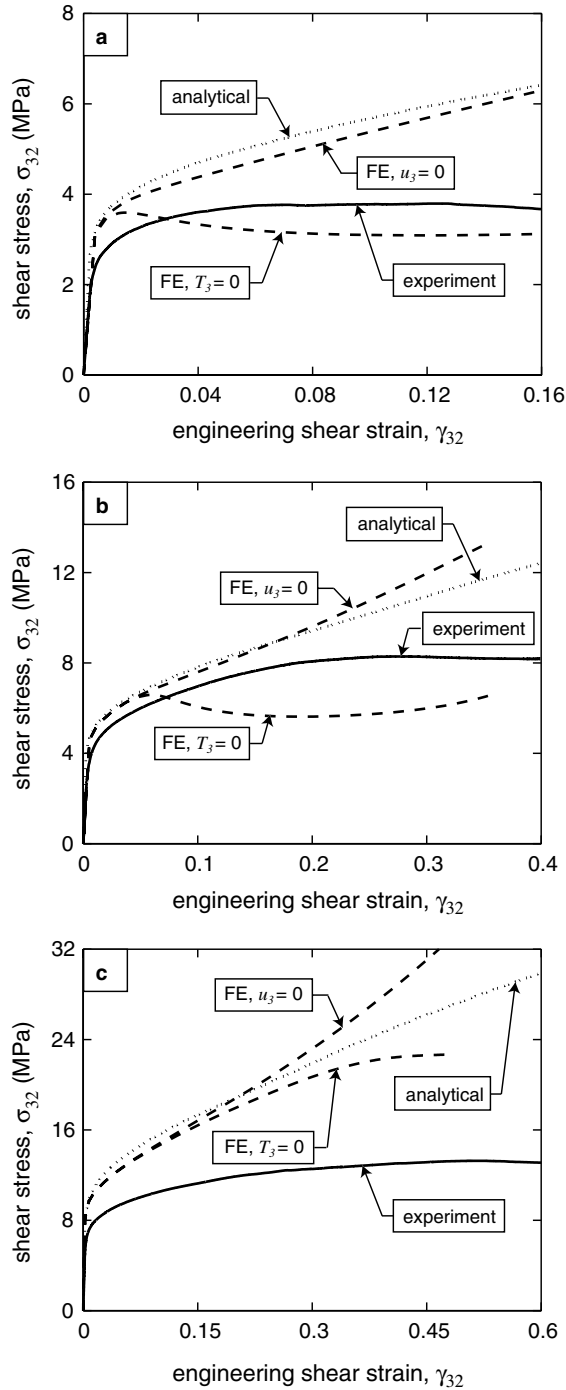
Fig. 10. Measured responses, finite element predictions and analytical predictions (Eq. (12)) of the corrugated core specimens in longitudinal shear: (a) $\bar{\rho} = 0.036$, (b) $\bar{\rho} = 0.05$ and (c) $\bar{\rho} = 0.10$. Finite element predictions for both the fully constrained grip condition ($u_3 = 0$) and the unconstrained grip condition ($T_3 = 0$) are included (an imperfection in the first eigenmode and maximum amplitude equal to 25% of the sheet thickness was specified in the FE calculations).
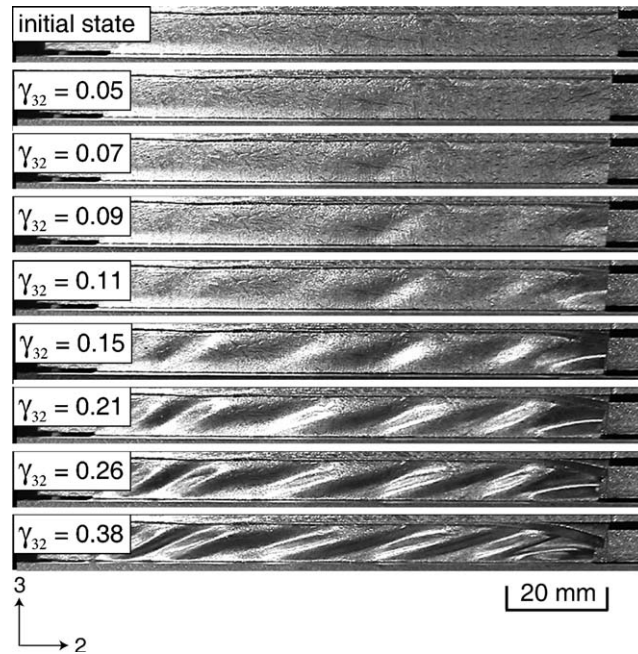
Fig. 11. Photographs of the $\bar{\rho} = 0.05$ corrugated core showing the deformation mode during tests in longitudinal shear.

respectively. Here, $E_t \equiv \mathrm{d}\sigma_s/\mathrm{d}\varepsilon_s$ is the tangent modulus of the plane strain true tensile stress versus logarithmic strain curve of the parent material evaluated at $\sigma_s = \sigma_c$, and σ_y its yield strength. Note that the von-Mises yield criterion and flow rule dictate that the plane strain yield stress is related to the plane stress tensile. stress by, $\sigma_s = 2\sigma/\sqrt{3}$, and the work conjugate strain to σ_s is related to the plane stress tensile strain by, $\varepsilon_s = \sqrt{3}\varepsilon/2$. The factor k depends upon the end-constraints of the struts. For the corrugated core it is reasonable to assume the struts be built-in, giving $k = 2$. In general, Eq. (8) needs to be solved numerically with the measured tensile response of the parent material used to define E_t. In the case of an ideally plastic material, Eq. (8) reduces to

$$\sigma_c = \begin{cases} \dfrac{k^2\pi^2 E_s}{12(1-v^2)}\left(\dfrac{t}{l}\right)^2 & \text{if } \dfrac{t}{l} < \sqrt{\dfrac{8\sqrt{3}(1-v^2)\sigma_y}{\pi^2 k^2 E_s}}, \\[4mm] \dfrac{2\sigma_y}{\sqrt{3}} & \text{otherwise.} \end{cases} \tag{9}$$

It remains to develop a relation for the longitudinal shear strength of the corrugated core. In case of an elastic ideally plastic parent material, the peak longitudinal strength of the corrugated core is given by

$$\sigma_{32}^{\mathrm{p}} = \begin{cases} \dfrac{3\pi^2 E_s}{4(1-v^2)\cos\omega}\left(\dfrac{t}{l}\right)^3 & \text{if } \dfrac{t}{l} < \sqrt{\dfrac{4(1-v^2)\sigma_y}{3\sqrt{3}\pi^2 E_s}}, \\[4mm] \dfrac{\sigma_y}{\sqrt{3}\cos\omega}\dfrac{t}{l} & \text{otherwise,} \end{cases} \tag{10}$$

where we have employed the prediction of Timohensko and Gere (1961) for the elastic buckling of thin plates. In case of a strain hardening parent material response, we can only provide analytical expressions

for the shear stress versus strain response of the corrugated core prior to the development of wrinkles (i.e. when the constituent sheets are in a uniform state). With the engineering shear strain γ_w in the walls of the corrugated core related to the macroscopic applied strain γ_{32} via Eq. (4), the principle of virtual work implies that the corresponding wall stress τ_w is given by

$$\tau_{32} = \tau_w \bar{\rho} \sin \omega. \tag{11}$$

The longitudinal shear stress versus strain response (τ_{23} versus γ_{23}) follows from the solid material tensile response as

$$\tau_{32} = \begin{cases} \dfrac{E_s}{2(1+v)} \bar{\rho} \sin^2 \omega \gamma_{32} & \text{if } \gamma_{32} < \dfrac{2(1+v)\sigma_y}{\sqrt{3} E_s \sin \omega}, \\ \dfrac{\bar{\rho} \sin \omega}{\sqrt{3}} \sigma(\varepsilon_{ref}) & \text{otherwise}, \end{cases} \tag{12}$$

where $\varepsilon_{ref} \equiv \gamma_{32} \sin \omega / \sqrt{3}$ and $\sigma(\varepsilon)$ is the uniaxial true stress logarithmic strain curve of the solid material. It is emphasized that this analysis assumes uniform deformation of the corrugated core. Thus, the analysis provides an upper bound to the strength of the corrugated core and does not predict the peak shear strength set by wrinkling of the corrugated core sheets.

3.2. Finite element analysis

Finite element calculations of the compressive and shear response were performed using the general purpose finite element package ABAQUS (HKS—*Hibbitt, Karlsson & Sorensen, Inc.*). It suffices to model a single corrugation, modelled using 3-dimensional linear shell elements (S4R in the ABAQUS notation). All degrees of freedom (translational and rotational) of the nodes at the base of the unit cell were fully constrained, while only the rotational degrees of freedom of nodes at the apex of the unit cell were constrained. Displacements were applied uniformly to the nodes at the apex of the unit cell to simulate the compression or shear of the core. Typically, the model comprised 100 shell elements in the x_2-direction and 40 elements along the length of the struts: giving a total of 8000 linear shell elements.

The uniaxial true stress versus logarithmic plastic strain was tabulated in ABAQUS using the experimentally measured response (Fig. 5). For the compression and transverse shear calculations, an imperfection in the shape of the buckling mode was imposed onto each strut. The imperfection is described by an initial transverse deflection w

$$w(s) = \frac{\zeta t}{2} \left[1 - \cos \left(\frac{2\pi s}{l} \right) \right], \tag{13}$$

where ζ is a dimensionless imperfection parameter and s the arc length along the strut measured from one end. Similarly, in the longitudinal shear calculations, an imperfection in the first eigenmode and maximum amplitude equal to 25% of the sheet thickness was specified in the FE calculations.

In the out-of-plane compression calculations, displacements were prescribed in the x_3-direction, uniformly at all the nodes on the apex of the unit cell, with the tractions, T_1 and T_2 (in the x_1- and x_2-directions, respectively) set equal to zero (natural boundary conditions for displacement-based variational problems). Similarly, loading in the transverse and longitudinal shear simulations was applied through prescribed displacements in the x_1- and x_2-directions respectively, applied uniformly to all nodes on the apex of the unit cell with the traction $T_3 = 0$. An additional set of shear simulations was performed with the displacements $u_3 = 0$ specified on all nodes on the apex of the unit cell. We shall refer to the simulations with

tractions $T_3 = 0$ as *unconstrained* while the simulations with $u_3 = 0$ as *constrained*. These choices should bound the measured responses.

3.3. Comparison between predictions and measurements

3.3.1. Out-of-plane compression

Comparisons between the finite element predictions and measurements (Fig. 6) reveal that the post-peak response is captured accurately for both choices of the imperfection magnitude, $\zeta = 0.01$ and 0.25. However, only the $\zeta = 0.25$ simulations predict the peak stress accurately. This level of imperfection corresponds to a transverse deflection of 0.075 mm in the struts, consistent with the imperfections introduced during manufacture. The analytical calculations (Eq. (8)) over-predict the peak strength (Fig. 12a) because they
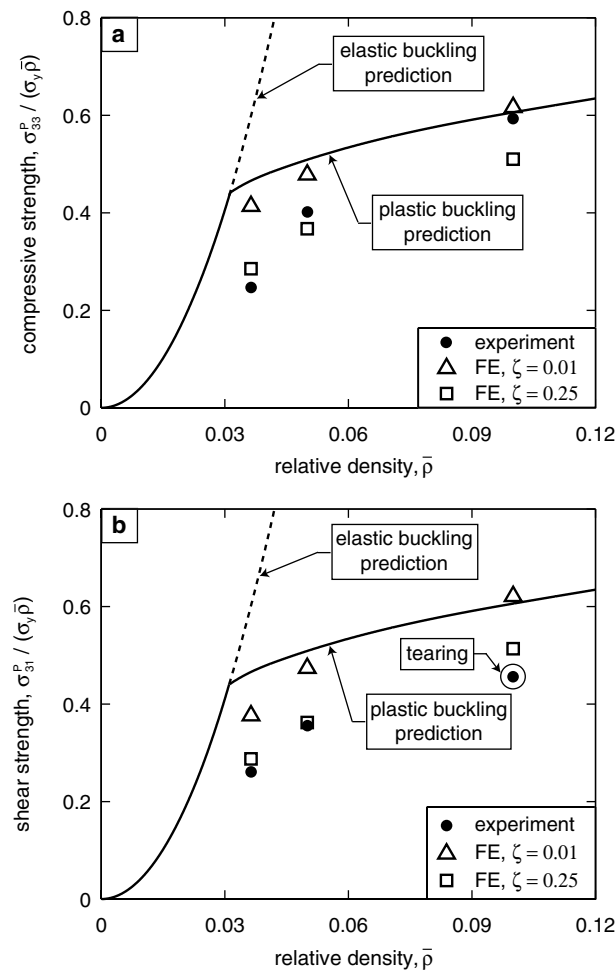

Fig. 12. A comparison of the measured and predicted peak values of (a) out-of-plane compressive strength, and (b) transverse shear strength of the corrugated core as a function of the relative density. The solid lines give the analytical predictions of the elastic buckling and plastic buckling strengths. Note that all strengths have been normalised by $\sigma_y \bar{\rho}$.

do not include imperfections; the inclusion of such imperfections within the FE calculations rectifies the discrepancy.

3.3.2. Transverse shear

The constrained and unconstrained FE simulations ($\zeta = 0.25$) of the response are included in Fig. 8 along with the measurements. The unconstrained simulations capture the peak strength but under-predict the post-peak stress. The constrained calculations predict a hardening response at stresses substantially larger than the measurements. The measured response is intermediate between the constrained and unconstrained simulations. This suggest that the grips provide some constraint against displacement in the x_3-direction. Consistent with out-of-plane compression, the analytical calculations and FE simulations with $\zeta = 0.01$ over-predict the peak strength (Fig. 12b) while the $\zeta = 0.25$ simulations accurately capture the measurements.

3.3.3. Longitudinal shear

A comparison between the analytical predictions with strain hardening (Eq. (12)), FE simulations and measurements (Fig. 10) indicate that the analytical predictions are in good agreement with the constrained simulations. Again, the measured responses for the $\bar{\rho} = 0.036$ and 0.05 cores are between the unconstrained and constrained predictions, consistent with lateral constraint from the grips. For the core with $\bar{\rho} = 0.10$, the analytical model and both FE simulations predict an almost identical response up to $\gamma_{32} \approx 0.3$. However, the measured response is much weaker due to tearing of the core from the face-sheets.

4. Diamond core

The out-of-plane compressive responses (Fig. 13) reveal large oscillations associated with the sequential collapse and lock-up of successive layers of the core. The sequence of events is evident from the images (Fig. 14). The transverse shear responses are plotted in Fig. 15 for $L/H = 8$. For comparison purposes, the corresponding compression data from Fig. 13 are included. Whilst the peak strengths in compression and transverse shear are approximately equal, the post-peak responses differ. Images of a progressively deformed transverse shear specimen (Fig. 16) indicate an absence of successive deformation bands. Rather, rupture occurs in the struts inclined at $\theta = 45°$ with respect to the x_1-direction.

4.1. Analytical models for the compressive and shear response

Zupan et al. (2004) developed expressions for the stiffness and strength of the woven sandwich core. Expressions for the stiffness and strength of the diamond core may be obtained in a similar manner. Details of the derivations are omitted and the reader is referred to Zupan et al. (2004).

Assuming plane-strain deformation, the out-of-plane compressive and transverse shear moduli are

$$E_{33} = \frac{E_s}{1 - v^2}\left(1 - \frac{1}{(L/H)\tan\omega}\right)\bar{\rho}\sin^4\omega, \tag{14}$$

and

$$G_{31} = \frac{E_s}{1 - v^2}\left(1 - \frac{1}{(L/H)\tan\omega}\right)\frac{\bar{\rho}}{4}\sin^2 2\omega, \tag{15}$$
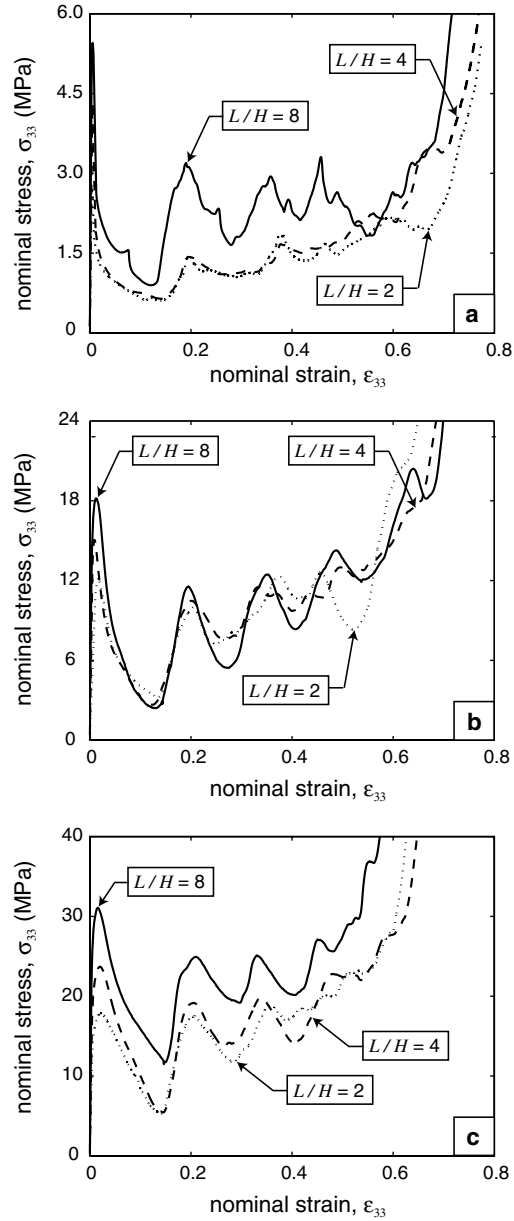
Fig. 13. Measured out-of-plane compressive response of diamond core specimens with aspect ratios $L/H = 2$, 4 and 8: (a) $\bar{\rho} = 0.08$, (b) $\bar{\rho} = 0.19$ and (c) $\bar{\rho} = 0.25$.

respectively. Here, E_s is the Young's modulus of the parent material of the diamond core and ω is the cell angle. The out-of-plane compressive and transverse shear peak strengths are

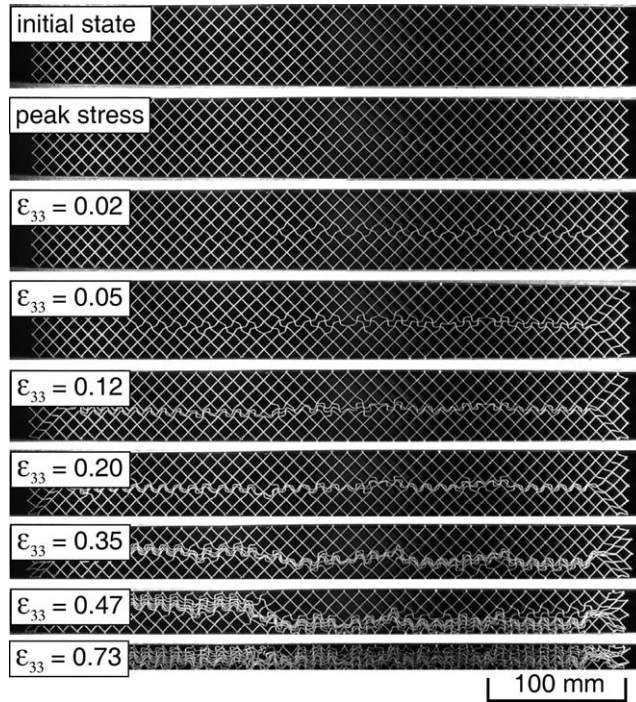$$\sigma_{33}^{p} = \sigma_c \left(1 - \frac{1}{(L/H)\tan\omega}\right)\bar{\rho}\sin^2\omega, \tag{16}$$

Fig. 14. Photographs of the $\bar{\rho} = 0.08$ diamond core showing the deformation mode during tests in out-of-plane compression.

and

$$\sigma_{31}^{\mathrm{p}} = \sigma_{\mathrm{c}} \left(1 - \frac{1}{(L/H)\tan\omega} \right) \frac{\bar{\rho}}{2} \sin 2\omega, \tag{17}$$

respectively, where σ_{c} is the maximum compressive strength of a constituent strut is set by the elastic or plastic buckling given by Eqs. (8) and (9). The weakest buckling mode corresponds to that for pin-ended plates of length, l, consistent with the buckling mode observed in Fig. 14. Thus, we set $k = 1$ in Eqs. (8) and (9).

4.2. Finite element analysis

Finite element calculations of the compressive and transverse shear responses were performed using the general purpose finite element package ABAQUS (HKS—*Hibbitt, Karlsson & Sorensen, Inc.*). Here the entire specimen was modelled using 3-dimensional linear shell elements (S4R in the ABAQUS notation). All degrees of freedom (translational and rotational) of the nodes on the bottom surface of the specimen were fully constrained while only the rotational degrees of freedom of nodes on the top surface were constrained. In addition, the translational degrees of freedom of the nodes on the top surface were constrained to be equal in order to simulate the bonding to the rigid face-sheet. Typically, each strut of the diamond core was discretised into 20 elements along its length, l, and in the x_2-direction.

The uniaxial true stress versus logarithmic plastic strain was tabulated in ABAQUS using the experimentally measured response (Fig. 5). An imperfection in the shape of the buckling mode was imposed onto each strut. The imperfection is described by an initial transverse deflection w
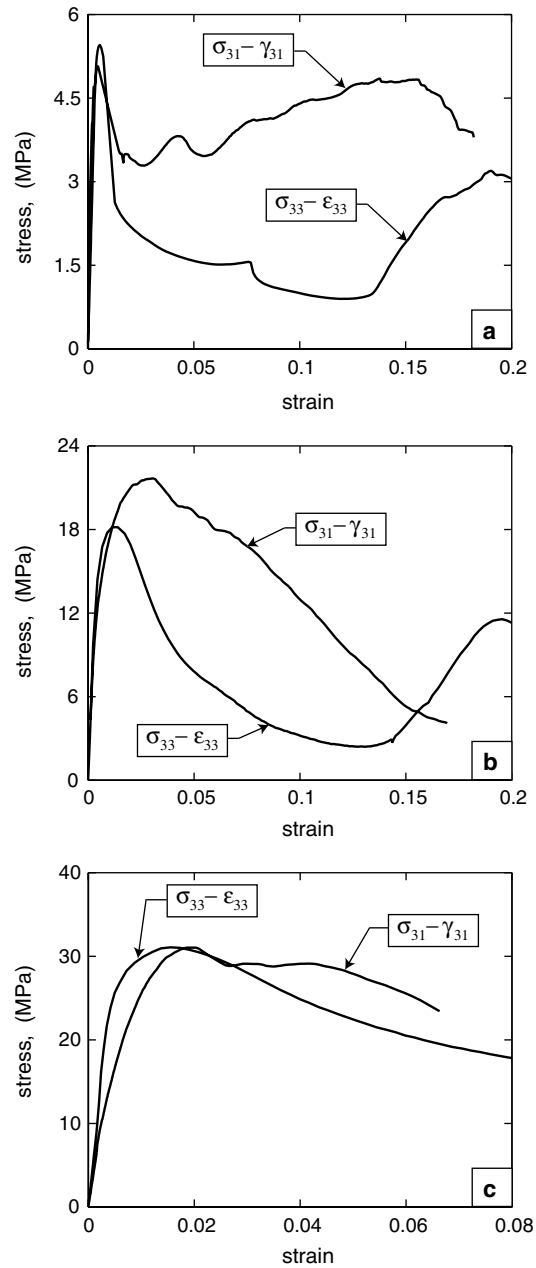
Fig. 15. A comparison of the out-of-plane compressive and transverse shear responses of the $L/H = 8$ diamond core specimens: (a) $\bar{\rho} = 0.08$, (b) $\bar{\rho} = 0.19$ and (c) $\bar{\rho} = 0.25$.

$$w(s) = \zeta t \sin\left(\frac{\pi s}{l}\right),$$
(18)

where ζ is a dimensionless imperfection parameter and s the arc length along a strut measured from one end. This imperfection corresponds to an Euler pin-ended struts buckling mode as the primary elastic
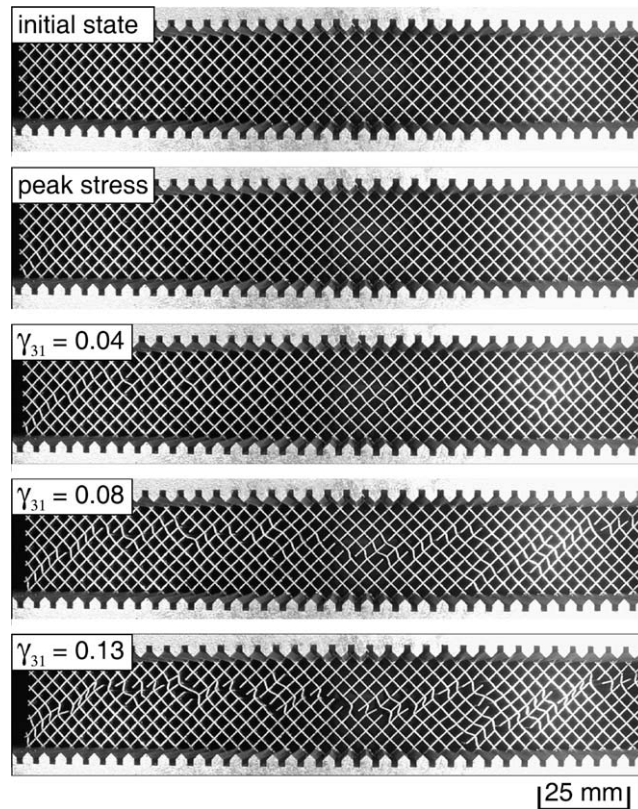
Fig. 16. Photographs of the $\bar{\rho} = 0.19$ diamond core showing the deformation mode during tests in transverse shear.

buckling mode of the diamond core that involves the rotation of the diamond core joints. By contrast, an imperfection (13) is employed in the corrugated core analysis as the sheets of the corrugated core are clamped at the rigid faces and hence the primary buckling mode in that case is that of an Euler clamped–clamped strut.

In the compression calculations, displacements were prescribed in the x_3-direction to the top surface with the tractions, T_1 and T_2 (in the x_1- and x_2-directions, respectively) set equal to zero (natural boundary conditions for displacement-based variational problems). Similarly, loading in the transverse shear simulations was applied through prescribed displacements in the x_1-direction, applied to the top surface with the tractions $T_3 = T_2 = 0$. This corresponds to the unconstrained case reported in Section 3.2. Consistent with the comparison between the FE predictions and measurements in Section 3.3, this boundary condition is thought to be the more realistic for the single lap shear experiments.

4.3. Accuracy of predictions

A comparison between the analytical predictions and the measured values of peak out-of-plane compressive strength (Fig. 17a) indicates that, while the trends are consistent, the analysis over-predicts the strength: this discrepancy is again attributed to the presence of imperfections. The FE predictions of the peak compressive strength for an imperfection value $\zeta = 0.1$ are included in Fig. 17b. These agree well with the measurements and confirm this suggestion.
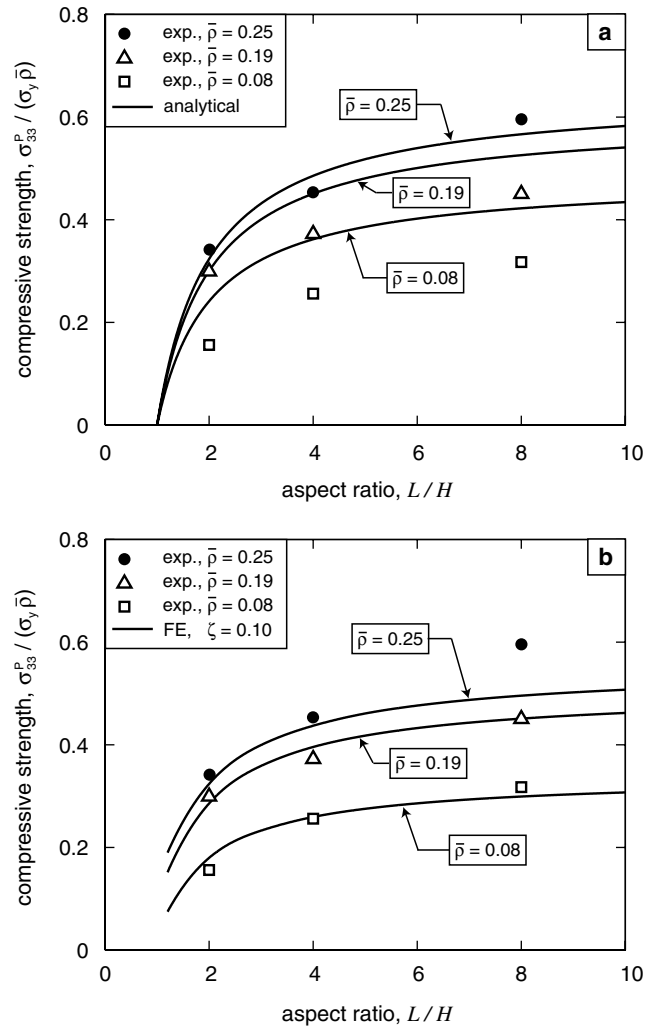
Fig. 17. A comparison of the measured and predicted peak compressive strengths of three relative densities of the diamond core. Experimental measurements versus (a) analytical and (b) FE ($\zeta = 0.1$) predictions.

In transverse shear (Fig. 18) good agreement between the analytical predictions, FE simulations ($\zeta = 0.1$) and measurements is apparent for $\bar{\rho} > 0.1$. Note that $\bar{\rho} = 0.08$ represents the transition between elastic and plastic buckling; where the imperfection sensitivity is greatest (see Hutchinson, 1974, for a detailed discussion) and here the measured peak shear strength is much less than the analytical and FE predictions.

5. Comparison of corrugated and diamond cores with competing core designs

It is instructive to compare the performance of the corrugated and diamond cores with competing cores. The dependence of peak compressive strength σ_p and shear strength τ_p upon relative density is summarized in Fig. 19. These figures include data for 304 stainless steel square-honeycombs (Côté et al., 2004), AL6XN stainless steel pyramidal cores (Zok et al., 2004; Côté, 2005) and aluminum alloy metal foams (Ashby et al.,
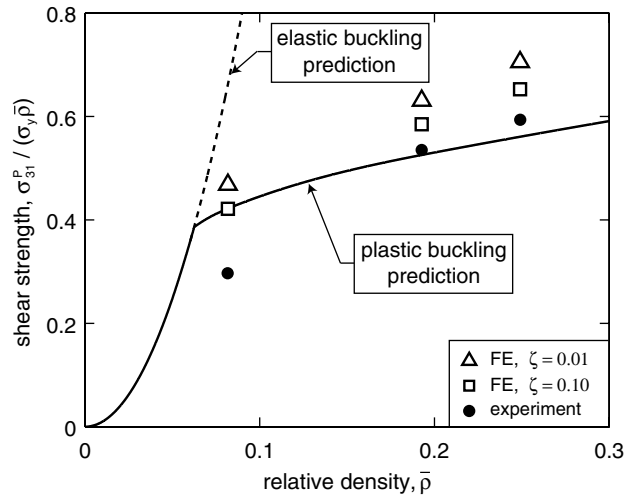
Fig. 18. Comparison between measurements, analytical and FE predictions of the transverse shear strength of the diamond core as a function of relative density $\bar{\rho}$, for $L/H = 8$.

2000). Note that the strengths have been non-dimensionalised by the factor $\sigma_y\bar{\rho}$. A value of $\sigma_p/(\sigma_y\bar{\rho})$ equal to unity is the maximum achievable in the absence of strain hardening. However, these austenitic stainless steels can strain harden appreciably enabling the non-dimensional strength $\sigma_p/(\sigma_y\bar{\rho})$ to exceed unity for the square honeycomb.

It is noted from Fig. 19a that the corrugated and diamond cores have a higher peak strength than metal foams but are weaker than the square-honeycombs. The square-honeycombs has exceptional strength because the core members are aligned with the loading direction and contain few manufacturing imperfections enabling the cells to undergo plastic buckling in a axial–torsional mode, see Côté et al. (2004). In contrast, the corrugated and diamond cores are misaligned with the loading direction and collapse by weaker plastic buckling modes.

The shear strengths τ_p of the various cores, defined by the peak stress in transverse shear, are compared in Fig. 19b. In longitudinal shear of the corrugated and square-honeycomb cores there is no peak; consequently, the strength is defined by the shear stress at 5% engineering shear strain. The longitudinal shear strength of the corrugated core is comparable to that of the square-honeycomb with $\tau_p/(\sigma_y\bar{\rho})$ approximately equal to its optimum value of 0.5 (assuming the Tresca yield criterion). In transverse shear, the corrugated and diamond cores are weaker than the square-honeycomb.

The compressive and shear energy absorption capacities of the corrugated and diamond cores are compared with those of competing sandwich core topologies in Fig. 20a and b, respectively. Here, the compressive and shear energy absorption capacities are defined by

$$W_c = \int_0^{\bar{\varepsilon}} \sigma \, d\varepsilon \tag{19}$$

and

$$W_s = \int_0^{\bar{\gamma}} \tau \, d\gamma, \tag{20}$$

respectively, where σ and τ are the compressive and shear stresses, and ε and γ are the work-conjugate strains. The energy absorption capacities are calculated up to the practical limits of strain $\bar{\varepsilon} = \bar{\gamma} = 0.5$. The normalisations of energy used in plotting Fig. 20 are chosen such that the non-dimensional compressive and shear
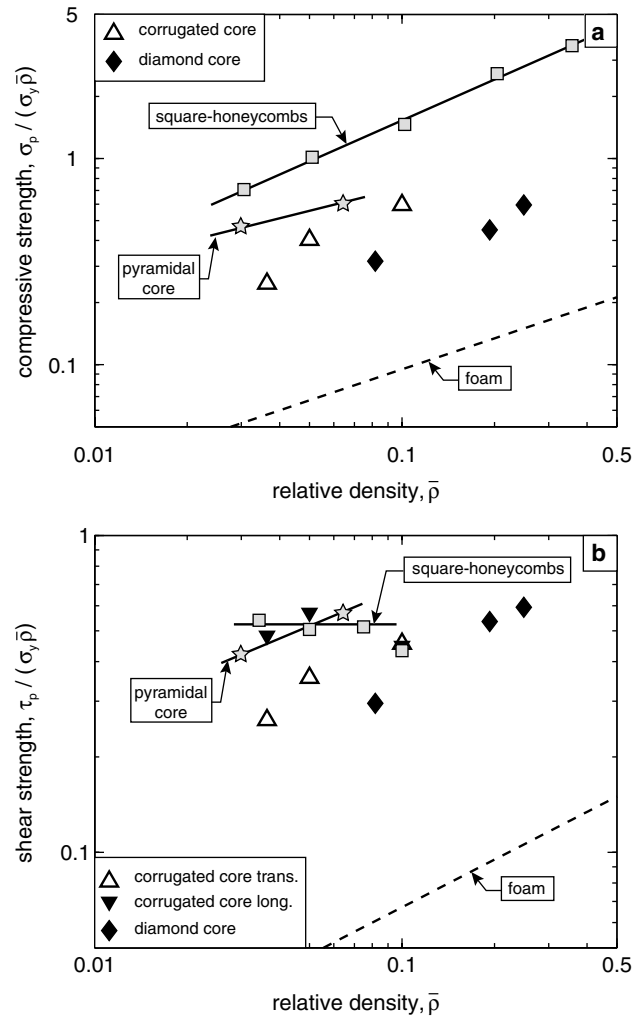
Fig. 19. A comparison of the measured peak strengths of competing sandwich cores as a function of the relative density: (a) out-of-plane compression and (b) transverse and longitudinal shear.

energy absorption capacities of sandwich cores made from an ideally plastic material of yield strength σ_y are equal to 1 and 0.5, respectively. The soft post-buckling responses of the corrugated and diamond cores in out-of-plane compression and transverse shear result in lower energy absorptions W_c and W_s than for the square-honeycomb and pyramidal sandwich cores. However, in longitudinal shear the non-dimensionalised value of W_s of the corrugated core approaches the optimal value of 0.5 and is comparable to that of the square-honeycomb.

6. Concluding remarks

Prismatic corrugated and diamond cores have been manufactured by slotting together sheets of 304 stainless steel and then brazing together the assembly. Three relative densities of the corrugated core were
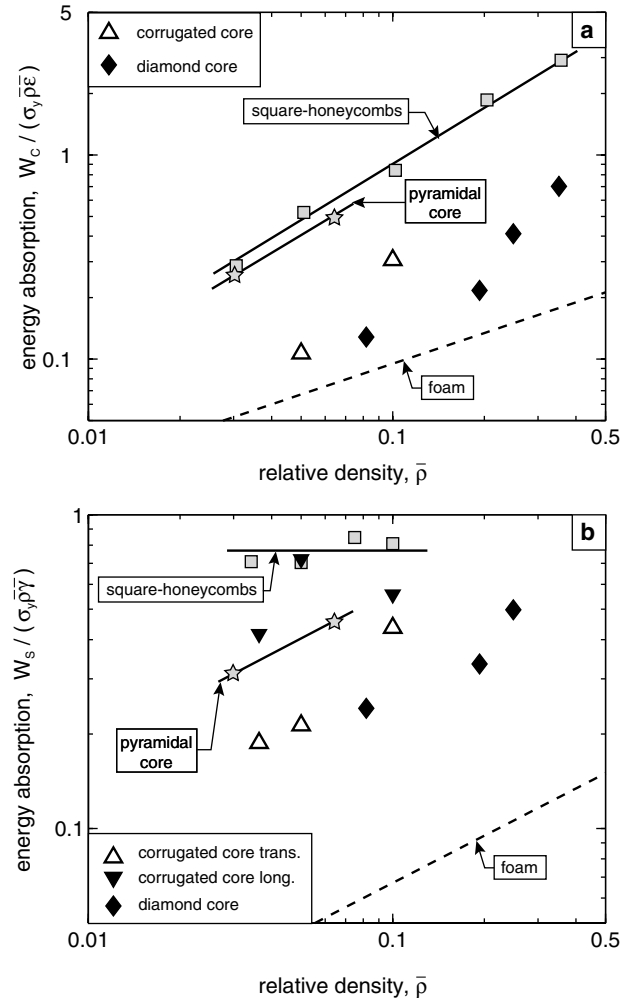
Fig. 20. A comparison of the measured energy absorption of competing sandwich cores as a function of the relative density: (a) out-of-plane compression and (b) transverse and longitudinal shear.

tested in compression and transverse as well as in longitudinal shear. By including geometric imperfections, the finite element models are in good agreement with the measured strengths while the analytical models (based upon the perfect microstructure) over-predict the measured strengths.

Three relative densities of the diamond cores were tested in out-of-plane compression and transverse shear. The compressive strength is sensitive to the aspect ratio of the specimen for aspect ratios less than about 4. Again, the measured strengths are below the analytical predictions due to geometric imperfections introduced during manufacture.

The prismatic cores have weak buckling modes under out-of-plane compression and shear and hence have lower strength to weight ratios than the square-honeycomb and pyramidal sandwich cores. However, the cores have a near optimal longitudinal shear strength and energy absorption capacity with $\tau_p/(\sigma_y\bar{\rho})$ and $W_s/(\sigma_y\bar{\rho}\bar{\gamma}) \approx 0.5$. Thus, prismatic cores have high potential for application in sandwich beam construction.

Acknowledgements

References

Ashby, M.F., Evans, A.G., Fleck, N.A., Gibson, L.J., Hutchinson, J.W., Wadley, H.N.G., 2000. Metal Foams: A Design Guide. Butterworth Heinemann.

Astech Inc., Innovative structural materials for the marine industry, Santa Ana, CA 92705, USA.

ASTM Standard C273-94, 1994. Standard test method for shear properties of sandwich core materials. American Society for Testing and Materials.

Côté, F., 2005. Metallic lattice materials for sandwich cores. Ph.D. thesis, Cambridge University, UK.

Côté, F., Deshpande, V.S., Fleck, N.A., Evans, A.G., 2004. The out-of-plane compressive behaviour of metallic honeycombs. Mater. Sci. Eng. A 380, 272–280.

Deshpande, V.S., Fleck, N.A., Ashby, M.F., 2001. Effective properties of the octet-truss lattice material. J. Mech. Phys. Solids 49, 1747–1769.

Evans, A.G., Hutchinson, J.W., Fleck, N.A., Ashby, M.F., Wadley, H.N.G., 2001. The topological design of multifunctional cellular metals. Prog. Mater. Sci. 46 (3–4), 309–321.

Fleck, N.A., Deshpande, V.S., 2004. The resistance of clamped sandwich beams to shock loading. J. Appl. Mech., ASME 71, 386–401.

Hutchinson, J.W., 1974. Plastic buckling. In: Yih, C.-S. (Ed.), Advances in Applied Mechanics, vol. 14. Academic Press, pp. 67–144.

Naar, H., Kujala, P., Simonsen, B.C., Ludolphy, H., 2001. Comparison of the crashworthiness of various bottom and side structures. Marine Struct. 15, 443–460.

Shanley, F.R., 1947. Inelastic column theory. J. Aeronaut. Sci. 14, 261–267.

Timohensko, S.P., Gere, J.M., 1961. Theory of Elastic Stability. McGraw-Hill, New York.

Valdevit, L., Hutchinson, J.W., Evans, A.G., 2004. Structurally optimised sandwich panels with prismatic cores. Int. J. Solids Struct. 41, 5105–5124.

Wadley, H.N.G., Fleck, N.A., Evans, A.G., 2003. Fabrication and structural performance of periodic cellular metal sandwich structures. Comp. Sci. Tech. 63, 2331–2343.

Xue, Z., Hutchinson, J.W., 2004. A comparative study of impulse-resistant metal sandwich plates. Int. J. Impact Eng. 30, 1283–1305.

Zok, F.W., Waltner, S.A., Wei, Z., Rathbun, H.J., McMeeking, R.M., Evans, A.G., 2004. A protocol for characterizing the structural performance of metallic sandwich panels: application to pyramidal truss core. Int. J. Solids Struct. 41, 6249–6271.

Zupan, M., Deshpande, V.S., Fleck, N.A., 2004. The out-of-plane compressive behaviour of woven-core sandwich plates. Eur. J. Mech. A—Solid 23, 411–421.